Assessment of heat exchangers for the integration of concentrated solar energy into the catalytic hydrothermal gasification of biomass

Journal Article

Author(s):
Viereck, Sebastian; Keller, Jonas; Haselbacher, Andreas; Jovanovic, Zoran R.; Steinfeld, Aldo

Assessment of Heat Exchangers for the Integration of Concentrated Solar Energy into the Catalytic Hydrothermal Gasification of Biomass

Sebastian Viereck,[b] Jonas Keller,[a] Andreas Haselbacher,[a] Zoran R. Jovanovic,*[a] and Aldo Steinfeld[a]

Using concentrated solar energy to power a hydrothermal gasification (HTG) of biomass requires thermal energy storage (TES) to compensate for the inherent intermittence of solar irradiation. The energy transfer from the TES to the HTG process is accomplished through a heat-transfer fluid (HTF) passing through a heat exchanger (HX) incorporated into the salt-separation step of the HTG process. The HX performance determines the temperature profile inside the salt separator, thereby influencing the removal of the salts from the feedstock. In this work, we compare the performances of three HX types based on exploiting fluidized beds, porous media, and axially finned tubes. The effect of the HX configuration on the temperature profile inside the salt separator is assessed through CFD simulations considering pure water as the model feed to the separator. We find that all considered HX types could provide the desired temperature profile within the separator. However, the estimate for the power required to pump the HTF through the fluidized-bed HX is roughly two orders of magnitude higher than those for the axially finned tubular and porous-media HXs.

Introduction

Biomass is a renewable alternative to natural gas and crude oil as feedstock for the production of chemicals, fuels, and electricity.[1] The production of fuels from biomass, such as bioethanol and biodiesel, competes with agricultural resources for food production, thereby increasing food prices.[2] To be sustainable, biofuels must therefore be produced from non-food-grade biomass. One such category of biomass with its potential currently largely unexploited is so-called wet biomass, typically containing > 75 wt % of water[2c] that is either available as a by-product of other processes (e.g., sewage sludge and manure[1]) or grown under conditions not suitable for food production (e.g., microalgae[3]).

Because of its high water content, wet biomass cannot be efficiently converted into biofuels using established thermal biomass gasification processes.[1b,4] These processes require water contents in the feedstock below 20 wt % to achieve an energy-efficient gasification.[5] At higher water contents, substantial portions of the energy contained in the biomass would be consumed for its drying.[6] The evaporation of water can be avoided by carrying out the gasification under hydrothermal conditions, that is, at pressures high enough to keep the water in liquid or supercritical state at typical gasification temperatures of 673–773 K.[1a]

The hydrothermal gasification (HTG) process typically consists of three steps: (1) compression of the biomass to about 300 bar; (2) heating of the compressed biomass to temperatures in the range of 673–773 K, that is, above the critical point of water; and (3) catalytic conversion of the biomass to synthetic natural gas.[7] During the heating of the compressed biomass, the water becomes supercritical and starts behaving as a non-polar solvent. Salts present in the biomass (taken up either as nutrients or during handling of the biomass[8]) thus either separate as brine (type-1 salts) or precipitate as particles (type-2 salts).[9] Both type-1 salt brines and precipitated type-2 salt particles could poison the gasification catalysts.[1a,2a] The precipitated type-2 salt particles may, in addition, cause plugging of the catalyst bed and fouling of heat-exchange surfaces and downstream process equipment. Therefore, the salts that separate from the biomass during the heat-up have to be removed prior to gasification.

Because of the importance of effective salt removal for downstream unit operations, the heating step of the HTG process is commonly referred to as the salt-separation step. This process step also consumes most of the energy required to operate the HTG[5] that is conventionally provided by electricity or by burning either fossil fuels or a fraction of

[a] J. Keller, Dr. A. Haselbacher, Dr. Z. R. Jovanovic, Prof. A. Steinfeld
Department of Mechanical and Process Engineering
ETH Zürich
Sonneggstrasse 3
Zurich 8092 (Switzerland)
E-mail: zjovanovic@ethz.ch

[b] S. Viereck
Solar Technology Laboratory
Paul Scherrer Institute, Villigen PSI
Villigen 5232 (Switzerland)

the produced fuels. Exploiting renewable solar energy to heat the salt separator may thus improve both the yield and energy efficiency of the HTG process.[10] However, to operate the HTG process continuously despite the inherent intermittence of solar irradiation, a thermal energy storage (TES) system has to be employed to store solar energy and make it available as process heat when solar irradiation is insufficient. The energy transfer from the TES to the salt separator is accomplished by using a heat-transfer fluid (HTF) that passes the thermal energy to the salt separator through a heat exchanger (HX) fitted to the salt separator. One of the most convenient HTFs is air as it is readily available, nontoxic, and without a temperature limitation.

A HX for heating the salt separator should satisfy two requirements: (1) it should provide thermal power sufficient to heat the compressed biomass to the required gasification temperature and (2) it has to induce a temperature profile inside the salt separator that promotes an effective salt separation and removal. Presently, it is not possible to derive this temperature profile theoretically, so it needs to be determined experimentally. Schubert et al.[11] reported several temperature profiles along the centerline of an electrically heated, lab-scale dip-tube salt separator that led to effective separation of type-1 salts from aqueous solutions and removal of their brines. Yet, the authors provided no information about the corresponding axial temperature and heat-flux profiles or the heat-transfer rate at the heater/separator interface (HSI). At the same time, neither Schubert et al.[12] nor Peterson et al.[13] were able to identify conditions for effective type-2 salt separation in this separator configuration.

The objective of this work is to evaluate the ability of three common heat-exchange strategies to transfer thermal energy to the dip-tube salt separator in a way that results in effective separation of type-1 salts. It should be mentioned that the separation of type-1 salts pertains not only to the solar-driven HTG of feedstock that contains mainly type-1 salts (e.g., distiller's grain[14] or crude glycerol[15]); certain mixtures of type-2 salts also exhibit an overall type-1 phase behavior.[12, 16] The herein considered heat-exchange strategies were based on transferring the thermal energy from hot air to the separator by using a bed of fluidized particles, axially finned tubes, or porous media. Preliminary design of different configurations of these three HX types (where a configuration refers to a HX with defined geometry, dimensions, and operating conditions) were carried out using simple engineering calculations requiring only two inputs: (i) the axial temperature profile at the HSI and (ii) the heat-transfer rate to the HSI. In the absence of more relevant information, the HSI temperature was assumed to be axially uniform and correspond to one of the heater set-point temperatures reported by Schubert et al.[11] To validate this assumption we used computational fluid dynamics (CFD) simulations, which demonstrated good agreement between the computed and experimentally observed centerline temperatures. The simulations also enabled the calculation of the corresponding heat-transfer rate at the HSI. In reality, only the designed fluidized-bed HXs deliver the axially uniform tem-

perature profile at the HSI and thus match the targeted temperature profile along the centerline of the salt separator. Axially finned tubular and porous-media HXs deliver nonuniform axial temperature profiles at the HSI. For these HX types, coupled HX/separator CFD simulations were thus used to evaluate the effect of the axial non-uniformity of the HSI temperature on the centerline temperature profile and to refine the preliminary HX designs such that they too provide the targeted centerline temperature profile. Finally, the HX configurations were rated based on the heat-transfer effectiveness and power required to pump the HTF through the HX.

Dip-Tube Salt Separator

Description

The dip-tube salt separator used by Schubert et al.[11] and initially proposed by Hong et al.[17] is shown in Figure 1. A salt-containing feed, beforehand compressed to approximately 300 bar, enters through the dip tube and is heated to temperatures in the range of 673–773 K by the electrical heaters surrounding the separator vessel. The salts separate in the upper, supercritical zone of the separator and form a dense,
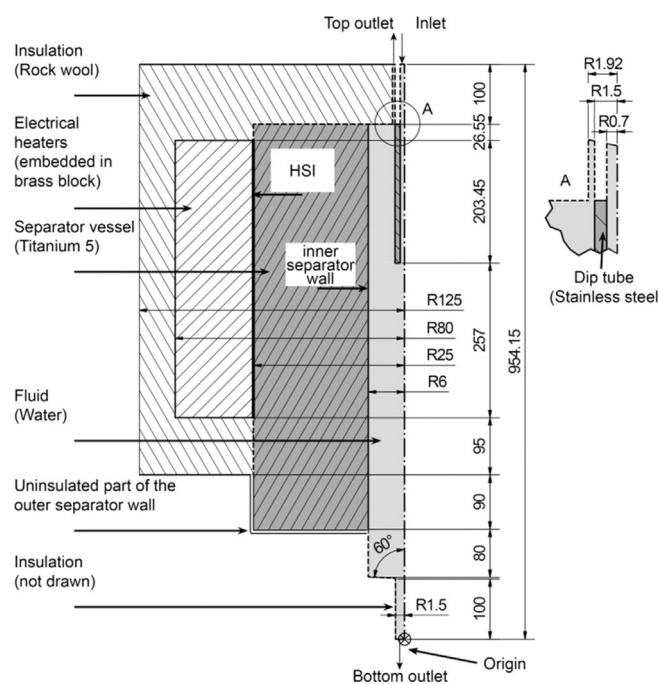

Figure 1. Illustration of the dip-tube separator. The dimensions of the separator vessel were taken from the drawings provided by SITEC-Sieber Engineering AG (Maur, Switzerland), the dimensions of the dip tube correspond to those reported by Schubert et al.[11] All dimensions are shown in millimeters. Radial dimensions are not to scale. The fluid domain, dip tube, and separator wall were scaled by a factor of 10 compared to axial dimensions; the heater and the insulation are drawn with arbitrary radial dimensions.

salt-rich phase that settles in the lower, subcritical zone, where it is withdrawn. The salt-depleted part of the feed reverses its flow direction because of buoyancy and leaves the separator at the top.

Assessment of the fluid flow and temperature field

For the particular configuration of the dip-tube salt separator illustrated in Figure 1, Schubert et al.[11] reported several heater set-point temperatures and corresponding centerline temperature profiles that effected separation of type-1 salts from aqueous solutions and removal of their brines. Schubert et al.,[11] however, did not provide axial temperature profiles and heat-transfer rates at the HSI. As this information is essential for the selection and design of a suitable HX, we inferred it as follows. We assumed that the temperature of the HSI was axially uniform and equal to one of the reported heater set-point temperatures, $T_{sp} = 723.15$ K. To check whether the assumed temperature profile at the HSI results in a temperature field inside the separator that effects salt separation, we used CFD (Ansys CFX 14.5.7[18]) to compute the temperature and flow field in the salt separator and then compared the computed to the measured centerline temperatures.

To reduce the computational costs of the CFD simulation, the salt-separator geometry was modified to be axially symmetric by replacing the originally lateral outlet at the top of the separator by an outlet of the same cross-sectional area arranged concentrically around the dip tube (see Figure 1). The simulated flow field near the top outlet thus differs from the flow field in the actual salt separator. However, this difference is considered to be acceptable as Peterson et al.[13a] showed for a similar salt separator that this area is not susceptible to salt deposition. Furthermore, the inlet and the outlets were extended 100 mm above and below the actual geometry of the salt separator to obtain fully developed flow profiles at the locations where the pressure-outlet boundary condition (BC) at the top outlet and the mass-flow outlet BCs at the inlet and bottom outlet, respectively, were defined.

The computational domain considered in the simulation is represented by the shaded areas in Figure 1; it consists only of the separator vessel, the dip tube, and the fluid domain. The separator vessel and the dip tube were assumed to be made from titanium grade 5 and stainless steel 316, respectively; water was assumed as the fluid phase as Schubert et al.[11] measured the centerline temperature profiles by feeding deionized water to the salt separator while keeping all other operating conditions similar to those found to be effective for type-1 salt separation. The three-dimensional geometry requirement imposed by CFX was met by considering a 2° revolute of the computational domain around the symmetry axis. Symmetry BCs were applied at the planes limiting the 2° slice in the circumferential direction. The BCs at the inlet, top outlet, and bottom outlet correspond to the experimental conditions reported by Schubert et al.[11] Insulated surfaces were modelled as adiabatic walls. The electrical heaters were represented by a temperature BC assigned to the HSI. The thermal energy lost at the uninsulated part of the outer separator wall was modelled as a convective–radiative heat loss; the convective heat-transfer coefficient between the outer separator wall and the surroundings and the

Table 1. BCs used to simulate the temperature and flow field of water in the salt separator.

Boundary	Line type (in Figure 1)	Condition[a]
inlet	NA	$\dot{m} = 1$ kg h^{-1} $T = 553.15$ K
top outlet	NA	$p = 300$ bar
bottom outlet	NA	$\dot{m} = 0.15$ kg h^{-1}
insulation (adiabatic wall)	– – – –	$q = 0$ W
HSI	——	$T_{HSI} = T_{sp} = 723.15$ K
convective-radiative heat loss	——	$q = h(T_{wall} - T_{\infty}) + \in \sigma(T_{wall}^4 - T_{\infty}^4)$ $h = 10.26$ W m^{-2} K^{-1} $\in = 0.45$ $T_{\infty} = 298.15$ K

[a] $\dot{m}$ is the flow rate, q is the heat flux, T_{HSI} is the temperature at the HSI, h is the convective heat-transfer coefficient between the outer separator wall and the surroundings, T_{wall} is the temperature at the part of the outer separator wall subject to convective–radiative heat loss, T_{∞} is the bulk temperature of the surrounding air, $\in$ is the hemispherical total emissivity of the outer separator wall, and σ is the Boltzmann constant. The line types associated with some of the boundaries correspond to the line types in Figure 1.

emissivity of the outer separator wall were taken from studies carried out by Macas,[19] who adjusted them to match the centerline temperature profiles experimentally determined by Schubert et al.[11] Numerical values of the BCs are given in Table 1. Further details about the model and its numerical implementation together with physical properties used in the simulation are enclosed in the Supporting Information.

Temperature and heat-transfer rate at the heater/separator interface

The simulated temperature profiles along the centerline and inner wall of the salt separator are compared with the measured centerline temperature profile[20] in Figure 2 (the measured data are provided in the Supporting Information). The simulation predicts the general trend of the measured centerline temperature profile reasonably well and even matches the value and axial position of its maximum. This means that assigning a temperature of 723.15 K to the HSI results in a temperature profile within the separator that would likely be effective for salt separation. Near the top of the salt separator, however, the measured temperatures along the centerline lie between the simulated values for the centerline and the inner wall. This deviation is attributed primarily to the difference of the arrangement of the top outlet used in the simulation compared to the one used in the experiment (as discussed in the previous section). Another possible explanation for the deviation might be that the thermocouple used to measure the centerline temperature was not perfectly aligned with the centerline but touched the inner wall of the salt separator at the top end.[21] The difference between the simulated and measured temperatures near the bottom
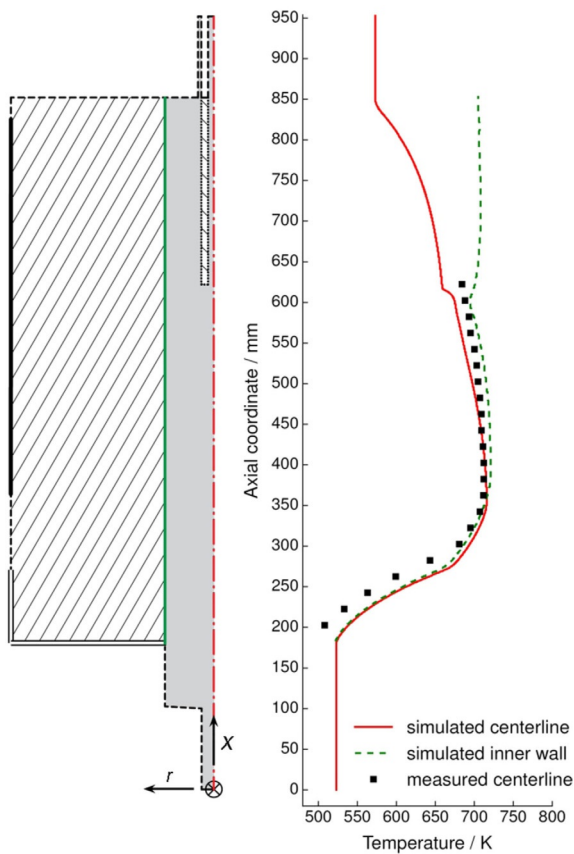
Figure 2. Comparison of measured centerline temperature profile (square symbols, raw data included in the Supporting Information)[20] with simulated centerline and inner-wall temperature profiles corresponding to an axially uniform HSI temperature of 723.15 K.

outlet is likely due to the uncertain parameters for the convective–radiative BC.

Integrating the heat flux over the HSI resulted in the target heat-transfer rate [Eq. (1)]

$$\dot{Q}_{\text{target}} = \int_s q \, \mathrm{d}S = -\int_S k_{\text{w}}(T) \frac{\mathrm{d}T}{\mathrm{d}r}\bigg|_{r=r_{\text{OW}}} = 359 \text{ W} \quad (1)$$

where S is the surface of the HSI, q is the heat flux at the HSI, k_{w} is the thermal conductivity of the separator wall (as given in the Supporting Information), T is the temperature, r is the radius, and r_{OW} is the radius of the HSI. The power required to pump the water through the salt separator was calculated as follows [Eq. (2)]

$$P_{\text{water}} = \int_A p\underline{U} \cdot \underline{n} \, \mathrm{d}A = 25.5 \text{ W} \quad (2)$$

where p, $\underline{U}$, $\underline{n}$, and A designate pressure, the velocity vector, the normal vector, and the boundary surface of the computational domain, respectively.

Preliminary HX Designs

Based on the simulation results summarized in Figure 2, a uniform axial temperature profile of the air at the HSI is likely to result in a centerline temperature profile that is in good agreement with the measured centerline temperature profile. However, the only conventional HX type that features such an air-temperature profile is the fluidized-bed HX because of the good mixing of particles and air. Fluidized beds, however, suffer from some operational issues such as particle attrition and erosion of the HX walls.[22] In addition, the effect of axial non-uniformity of the HSI temperature on the centerline temperature profile has not been assessed. Therefore, we decided to evaluate the suitability of two additional conventional HX types, porous-media HXs, and axially finned tubular HXs because they show a decrease in the axial temperature profile of the air from the inlet to the outlet. To simplify the design of these HXs and avoid considering the heat transfer inside the salt separator, which requires costly CFD simulations, the energy balance for air was approximated assuming the previously identified uniform axial temperature at the HSI. This assumption enabled identification of those configurations that delivered approximately the targeted heat-transfer rate of 359 W using either routine engineering HX design protocols or simple energy-equation models. The impact of this simplification was then assessed using CFD simulations of selected integrated HX/salt separator configurations to compute the actual temperature profiles at the HSI and at the centerline. The configurations were then refined such that their corresponding centerline temperature profiles matched the targeted centerline temperature profile corresponding to an HSI temperature of 723.15 K.

The schematics of the HXs integrated with the dip-tube salt separator are shown in Figure 3. As the HXs are in contact with the HSI, their inner diameters (d_i) are fixed. Their axial positions and heights are set to be identical to those of the electrical heater. Following Zanganeh et al.,[23] the inlet temperature of air was set to 823.15 K, as this corresponds to the outflow temperature of the air during discharging of a TES similar to that considered in the study of a solar-driven HTG process by Mian et al.[10] The air was assumed to exit the HX at ambient pressure, and the outer walls of the HXs were assumed to be adiabatic.

The approach to identify those HX configurations that approximately provide the targeted heat-transfer rate of 359 W comprised the following steps:

1. Identifying design parameters that influence the heat transfer from the HTF to the salt separator.
2. Defining ranges for each design parameter and dividing these ranges into suitable intervals to obtain a list of values for each parameter. Each combination of the elements of these parameter lists constitutes one HX configuration.
3. Selecting those configurations that deliver a heat-transfer rate of approximately 359 W. To do so, different ap-
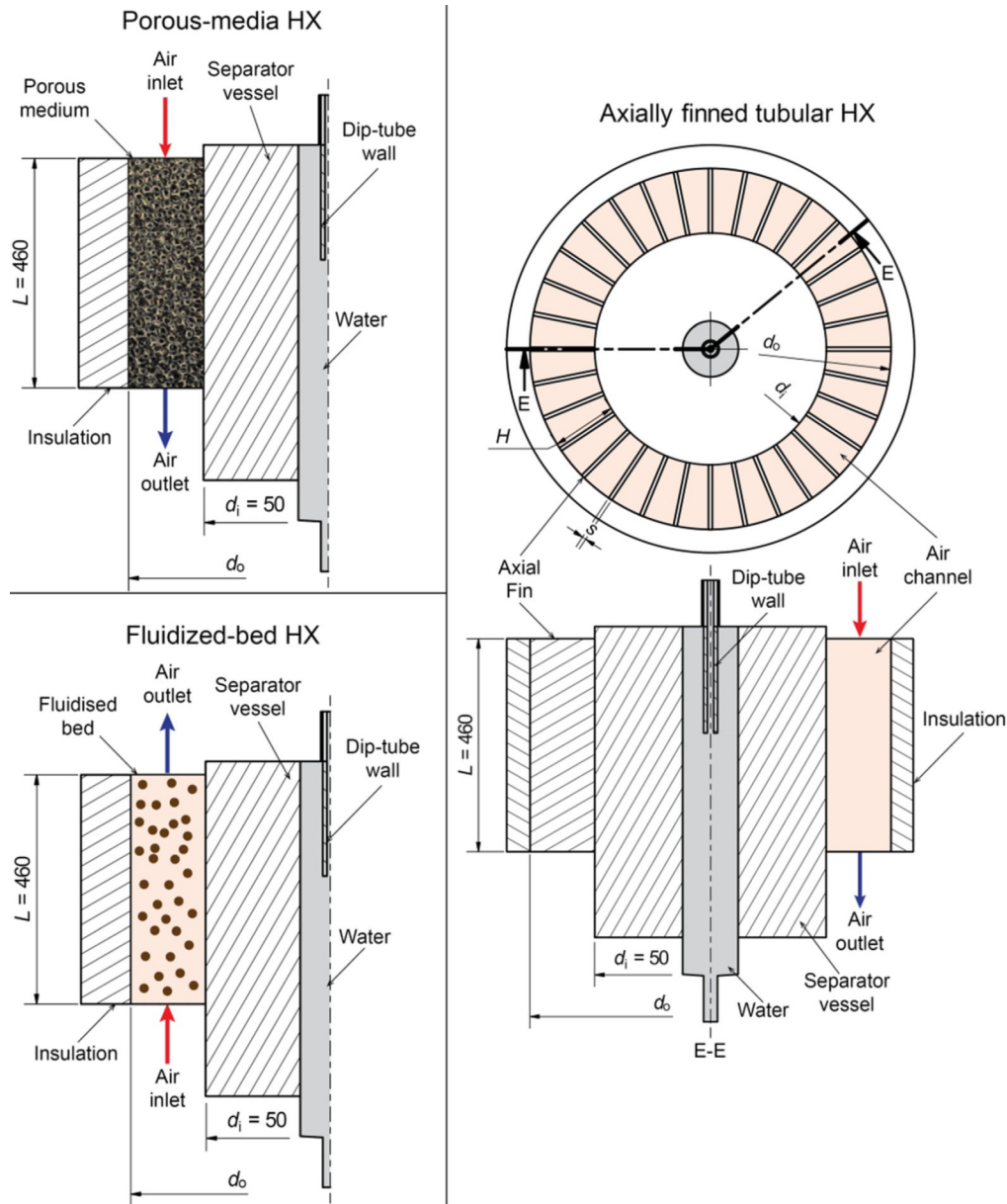
Figure 3. Schematic representations of the HX types considered in this study. The outer diameter is denoted with d_o, H is the fin height, and s is the fin thickness. The inner diameter d_i and the height L of the HSI are fixed. For the axially finned tubular HX, E-E denotes the plane through which the top view (upper right sketch) is cut to obtain the section view (lower right sketch). All dimensions in mm; radial dimensions are not to scale.

proaches were used for the different HX types; they are presented in the following sections.

For the preliminary design, constant physical properties of air corresponding to a temperature of 773.15 K and 1 bar pressure were used; they are tabulated in the Supporting Information. The selected HX configurations were compared using P_{air}, the power required to pump the air through the HX, and the heat-transfer effectiveness defined in Equation (3):[24]

$$\chi = \frac{\dot{Q}_{target}}{\dot{Q}_{max}} = \frac{\dot{Q}_{target}}{\dot{m} c_{p,g} \left(T_{g,in} - T_{HSI} \right)} \tag{3}$$

where $\dot{Q}_{max}$ is the maximum achievable heat-transfer rate, $\dot{m}_g$ is the air flow rate, $c_{p,g}$ is the specific heat capacity of air, and T_{HSI} is the temperature at the HSI.

For convenience, the power required to pump the air through the HX was normalized by the power required to pump the water through the salt separator [Eq. (4)]:

$$\Pi = \frac{P_{air}}{P_{water}} = \frac{\Delta p \dot{V}}{P_{water}} \tag{4}$$

where Δp and $\dot{V}$ are the pressure drop and the volumetric flow rate of air passing through the HX, respectively.

Fluidized-bed HX

There are several methods to calculate the bed-to-wall heat-transfer coefficient in a fluidized bed (Kunii and Levenspiel,[22] Yang[25]). In this work, the bed-to-wall heat-transfer coefficient was calculated using the equation suggested by Martin[26] (see the Supporting Information) based on the particle diameter (d_p), the voidage at minimum fluidization (ε_{mf}), and the bed voidage (ε). The bed voidage was calculated as a function of the superficial gas velocity (U_g) and the velocity at minimum fluidization (U_{mf}) using the equation suggested by Geldart (as cited by Yang,[25] equation 83, chapter 8.1) in combination with a particle mass balance and the equation for U_{mf} as a function of ε_{mf} given by Kunii and Levenspiel[22] (see the Supporting Information).

The design parameters d_p, ε_{mf}, and U_g were selected as follows:

1. The particle diameter was kept in the 50–250 μm range to ensure the bubbling fluidization regime, which features the highest bed-to-wall heat-transfer coefficients.[22] The particle diameter range was discretized in increments of 10 μm.
2. The voidage at minimum fluidization depends on the particle material and diameter. Because of their high thermal stability, we selected Al_2O_3 and SiC particles.[27] For simplicity, we assumed that the particles are spherical with constant physical properties (listed in the Supporting Information). We further assumed that the voidage at minimum fluidization does not vary over the considered particle-size range. The ε_{mf} values were therefore assumed to be 0.57 and 0.42 for SiC[27a] and Al_2O_3,[22] respectively.
3. The range of superficial gas velocities corresponding to the bubbling fluidization regime was reported by Yang[25] as function of the non-dimensional superficial velocity and non-dimensional particle size (see the Supporting Information). The upper and lower bounds of this non-dimensional velocity range were each fitted as functions of the dimensionless particle size, and the obtained ranges were then discretized in increments of 0.0001.

Assuming that the temperature difference between particles and air is negligible,[22] the required air flow rate and temperature in the bed (T_b) were obtained from the following two energy balances over the HX [Eqs. (5) and (6)]

$$\dot{Q}_{target} = \pi d_i L h (T_b - T_{HSI}) \tag{5}$$

$$\dot{Q}_{target} = \dot{m} c_{p,g} (T_{g,in} - T_b) \tag{6}$$

where h is the estimated bed-to-wall heat-transfer coefficient. The outer bed diameter (d_o) for every fluidized-bed HX configuration was then calculated from the air flow rate, superficial velocity, and diameter of the HSI according to Equation (7):

$$d_o = \sqrt{\frac{4\dot{m}_g}{\pi \rho_g U_g} + d_i^2} \tag{7}$$

where ρ_g is the density of air. The pressure drop over the fluidized bed was calculated for each configuration as Equation (8)[22]

$$\Delta p = L(1 - \varepsilon)(\rho_s - \rho_g)g \tag{8}$$

where ρ_s is the density of the bed material and g is gravity.

For a given heat-transfer effectiveness, there is more than one configuration that may deliver the required heat-transfer rate but at different pumping powers. As only the configuration with the lowest pumping power makes economic sense, Figure 4 shows only configurations requiring the lowest ach-
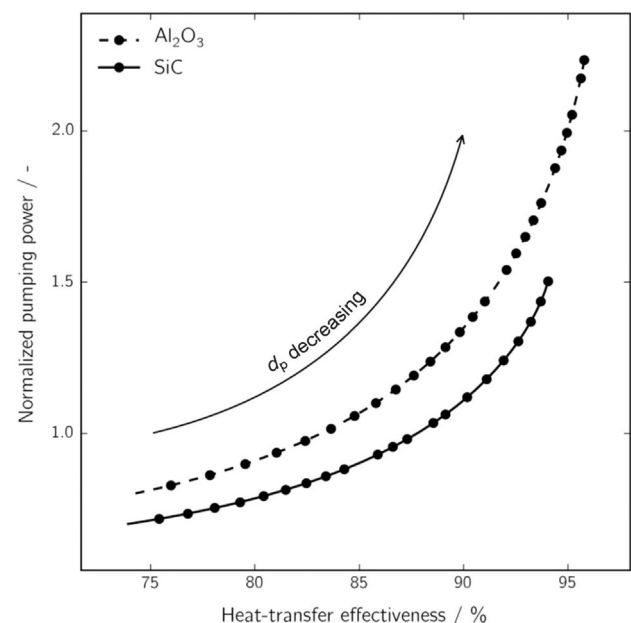

Figure 4. Normalized pumping power as a function of the heat-transfer effectiveness for the fluidized-bed HX configurations. Each symbol represents one fluidized-bed configuration (number of symbols reduced to improve readability of the graph). For a given heat-transfer effectiveness and particle material, only the configuration with the lowest pumping power is shown. HX configurations with smaller particle size achieve higher heat-transfer effectiveness but require more power to pump the air through the HX.

ievable pumping power for a given heat-transfer effectiveness and particle material. The following conclusions can be drawn from Figure 4:

1. Smaller particles lead to higher heat-transfer effectiveness as the bed-to-wall heat-transfer coefficient increases with decreasing particle size. Consequently, the bed temperature can be lower to achieve the targeted heat-transfer rate [see Equation (5)], which means that a lower air flow rate is sufficient to supply the required energy to the HX [see Equation (6)]. A lower air flow rate is equivalent to a higher heat-transfer effectiveness.

2. The configurations with higher heat-transfer effectiveness also require more power to pump the air. At higher heat-transfer effectiveness and consequently lower air flow-rates, the voidage of the bed decreases. Since we aimed at maintaining always the same height of the expanded bed to cover the entire HSI, the decreased bed voidage has to be compensated by a greater particle holdup. This increases the bed mass and thus the pressure drop in fluidized bed. The increase in pressure drop outweighs the reduction in the air flow rate; thus, the pumping power increases.

3. The configurations using SiC particles require lower pumping powers. Due to the lower density of SiC compared to Al_2O_3, the same particle holdup in the bed results in a lower bed mass and thus lower pressure drop.

4. Higher maximum heat-transfer effectiveness can be achieved with Al_2O_3 particles. The higher specific heat capacity and density of Al_2O_3 compared to SiC leads to a higher bed-to-wall heat-transfer coefficient and thus the desired heat-transfer rate can be achieved at a lower air flow rate.

Axially finned tubular HX

Heat transfer for the flow past an axially finned tube encompasses convective heat transfer in the channels between two adjacent fins and heat conduction through the fins. The corresponding overall heat-transfer coefficient and pressure drop were calculated as suggested by Kraus et al.[28] (see the Supporting Information). Within the range of conditions investigated, the flow regime of air was laminar; thus, the convective heat-transfer coefficient in the finned annulus was calculated from the corresponding constant Nusselt number for the case of convective heat transfer to a wall at constant temperature (as described in the Supporting Information).

Computing the heat-transfer rate from the HX to the salt separator and the outlet temperature of air was based on Equations (9) and (10):

$$\dot{Q} = \dot{m}c_{p,g}\left(T_{g,in} - T_{g,out}\right) \tag{9}$$

$$\dot{Q} = h_{\eta_0}A_{ht}\Delta T_m = h_{\eta_0}A_{ht}\left[\frac{\left(T_{g,in} - T_{HSI,hot}\right) - \left(T_{g,out} - T_{HSI,cold}\right)}{\ln\left(\frac{T_{g,in} - T_{HSI,hot}}{T_{g,out} - T_{HSI,cold}}\right)}\right] \tag{10}$$

where h_{η_o} is the overall heat-transfer coefficient and A_{ht} is the interfacial area available for heat transfer (as defined in the Supporting Information), ΔT_m is the logarithmic mean temperature difference, $T_{HSI,hot}$ and $T_{HSI,cold}$ are (generally speaking) the hot and cold temperatures at the HSI, and $T_{g,out}$ is the outlet temperature of the air. With the assumption of axially uniform temperature at the HSI ($T_{HSI,hot} = T_{HSI,cold} = T_{HSI}$), Equation (10) simplifies to Equation (11):

$$\dot{Q} = h_{\eta_0}A_{ht}\left[\frac{\left(T_{g,in} - T_{g,out}\right)}{\ln\left(\frac{T_{g,in} - T_{HSI}}{T_{g,out} - T_{HSI}}\right)}\right] \tag{11}$$

The considered configurations are based on commercially available axially finned tubes with an inner diameter of 50.8 mm (TECHNIFINR® TYPE "LFW", manufactured by TPS Technitube Röhrenwerke[29]). Stainless steel 316 was chosen as tube material; its physical properties are provided in the Supporting Information. These tubes are available with two numbers of fins ($N = 32$ and 40), two fin thicknesses ($s = 0.8$ and 1 mm), and fin heights ranging between $H = 6.4$ and 25.4 mm. The range of fin heights was discretized in increments of 0.1 mm. For every HX configuration, the air flow rate was adapted iteratively such that the targeted heat-transfer rate was achieved.

The normalized pumping power is plotted in Figure 5 as function of the heat-transfer effectiveness. This Figure implies the following:

1. Axially finned tubular HX configurations may attain heat-transfer effectiveness values that are as high as those estimated for fluidized-bed configurations.

2. The effectiveness increases with an increase in fin height. This is the combined result of several parameters being influenced by the fin height (see the Supporting Information for the definition of these parameters and Figure S1 showing the parameters as a function of the fin height):
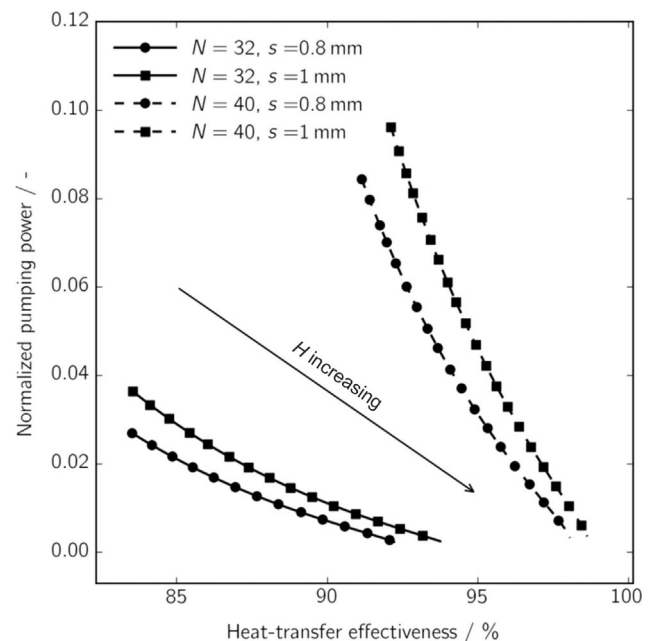

Figure 5. Normalized pumping power as a function of the heat-transfer effectiveness for the axially finned tubular HX configurations. Each symbol represents one configuration (number of symbols reduced to improve readability of the graph). HX configurations with higher fins (increasing H) have a higher effectiveness and lower pumping power.

a. The hydraulic diameter increases with fin height (H) as the cross-section available for air flow increases with H^2 but the wetted perimeter is linear in H.

b. The fin efficiency decreases with fin height. The fin efficiency is the ratio between the actual and the maximum heat flux between air and fin, the latter occurring if the entire fin would be at the temperature of its base (i.e., the HSI).[14] With increasing fin height, the temperature towards the tip of the fin gets closer to the air temperature. Consequently the additional fin surface does not contribute significantly to the heat transfer between air and fin, which results in a decrease in the fin efficiency.

c. For constant Nusselt number (laminar flow) and increasing hydraulic diameter, the convective heat-transfer coefficient decreases with increasing fin height. The overall heat-transfer coefficient, which is a product of convective heat-transfer coefficient and fin efficiency, $h_{\eta_o} = h\eta_o$, decreases as well.

d. The interfacial area between finned tube and air increases with increasing fin height.

The increase of the interfacial area overcompensates the decrease of the overall heat-transfer coefficient and thus the product $h_{\eta_o}A_{ht}$ increases with increasing fin height. For a constant heat-transfer rate, it can be inferred from Equation (11) that the air outlet temperature thus increases, which [according to Equation (9)] leads to a decrease in the air flow rate and thus an increase in the heat-transfer effectiveness.

3. The pumping power decreases with an increase in fin height. This is the combined result of the reduction in the required air flow rate (as explained above) for taller fins and the decrease in pressure drop. The latter decreases due to a decrease in air velocity provided by the reduced air flow rate and an increase in the flow cross-section.

4. Increasing the number of fins leads to both a higher maximum heat-transfer effectiveness and higher pumping power. An increase in the number of fins enlarges the air/tube interface and thus intensifies heat transfer. At the same time, the air velocity increases due to the decrease in the cross-sectional area available for air flow, which intensifies momentum transfer. Consequently, the desired heat-transfer rate is achievable at lower air flow rates but increased pressure drop.

5. Increasing the thickness of fins also leads to a larger air/tube interface and a lower cross-sectional area available for the air flow. As explained above, this leads to higher maximum heat-transfer effectiveness and higher pumping power.

Porous-media HX

In this type of HX, air flows through a porous medium filling the annulus between the HSI and the outer enclosure of the HX. The porous medium increases the gas–solid interfacial area, thereby enhancing the momentum and heat transfer.

Porous media can be manufactured from various materials such as metals, composites, and ceramics; they come in a variety of pore densities and porosities, which affect both heat transfer and pressure drop.[30] For the purpose of this work we represented the porous medium by a reticulated porous SiC (RP-SiC) because of its favorable thermo-mechanical stability, high thermal conductivity, and well-known physical properties.[31] The RP-SiC was assumed to have a porosity of 86 % and a pore density of 10 pores per inch (3.94 pores per cm),[31c] other properties are listed in the Supporting Information. For the results presented in this work, the outer diameter of the RP-SiC HX was varied between 0.06 and 0.25 m in increments of 1 cm. It was found that decreasing the outer diameter even further would only increase the pumping power but would not lead to a significant increase in the heat-transfer effectiveness. Similarly, a larger outer diameter would only decrease the heat-transfer effectiveness without significantly lowering the pumping power.

For each RP-SiC configuration associated with a certain outer diameter, the required air flow rate was determined iteratively such that the delivered heat-transfer rate would match the targeted value. For a given flow rate, the temperature profile in the HX was estimated by solving the non-equilibrium energy-equation model of Calmidi and Mahajan[32] using the commercial finite-element method solver SESES.[33] At the HSI, the temperature of 723.15 K was imposed as BC. The interfacial heat-transfer coefficient between the air and the RP-SiC was calculated using the correlation proposed by Pozivil et al.[31c] Having obtained the temperature field in the RP-SiC HX and thus knowing the outlet temperature of the air, the heat-transfer rate was calculated from the energy balance over the HX [Eq. (12)]

$$\dot{Q} = \dot{m}c_{p,g}\left(T_{g,in} - T_{g,out}\right) \tag{12}$$

If the calculated and targeted heat-transfer rate did not match, the air flow rate was adapted and the estimation of the temperature profile was repeated. The pressure drop was estimated by the Hazen–Dupuit–Darcy equation (page 10 in Ref. [34]). Details about the models and equations used to estimate the heat transfer and pressure drop for the RP-SiC configurations are provided in the Supporting Information. The normalized pumping power vs. heat-transfer effectiveness is shown in Figure 6

Heat transfer from the air to the salt separator increases with decreasing outer diameter due to faster radial heat conduction. Thus, a lower air flow rate is sufficient to provide the targeted heat-transfer rate. Hence, the heat-transfer effectiveness increases with decreasing outer diameter. For the pumping power, the decrease of the outer diameter and the air flow rate leads to two competing effects: pumping power decreases with decreasing air flow rate but the pressure drop increases as it is inversely proportional to the fourth order of the outer diameter. The latter becomes dominant as the outer diameter decreases, which explains the steep increase of the pumping power for higher heat-transfer effectiveness.
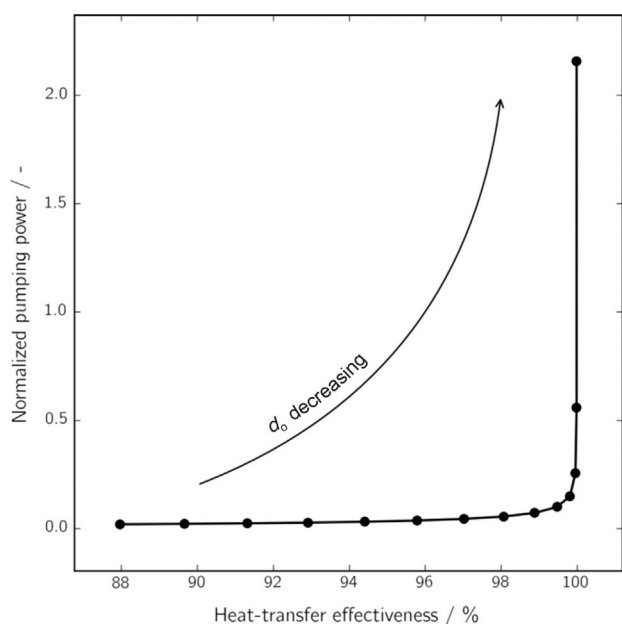
Figure 6. Normalized pumping power as a function of the heat-transfer effectiveness for the RP-SiC HX configurations. Each dot represents one RP-SiC configuration. Configurations with larger outer diameters lead to higher heat-transfer effectiveness and pumping power.

The computed temperature profiles were compared to the temperature profiles obtained from the simulation where a uniform temperature of 723.15 K was assigned to the HSI; the latter profiles are referred to as the target temperature profiles in the following. The outer-separator-wall and center-line temperature profiles simulated for the selected HX configurations are shown in Figures S2 and S3 in the Supporting Information, respectively. By the definition of the uniform BCs at the HSI, all fluidized-bed configurations result in the same temperature profile at the HSI and thus in the same centerline temperature profile. The investigated RP-SiC and axially finned HX configurations also result in similar temperature profiles at the outer separator wall and centerline.

Figure 7 shows the axial temperature profiles in the salt separator for the HX configurations demonstrating 95% heat-transfer effectiveness. The profiles are shown for four radial positions: the outer and inner separator wall, the radial position of the top outlet of the salt separator, and the centerline. Additionally, the target temperature profiles at these positions are shown as well. The fluidized-bed configuration provides exactly the targeted temperature at the HSI and thus also matches the centerline temperature profile. As expected, the RP-SiC and axially finned HX configurations

Performance Comparison of Integrated HX/Salt Separator Configurations

Centerline temperature profile

The preliminary designs for the axially finned tubular and PR-SiC HXs were obtained assuming a uniform air temperature at the HSI. However, in reality these HXs provide a non-uniform temperature profile. To assess how strongly the axially finned tubular and PR-SiC HXs deviate from the uniform temperature profile at the HSI and how this affects the corresponding centerline temperature profiles, we carried out integrated HX/salt separator simulations. The simulations were set up similar to those described earlier in this work. The integrated HX/separator simulations were restricted to the HX configurations resulting in heat-transfer effectiveness of 92%, 95%, and 96%. In case that a given effectiveness could be achieved with several configurations of the same HX type, the configuration with the lowest pumping power was chosen. The fluidized-bed configurations were included into the simulations by applying the corresponding heat-transfer coefficient and bed temperature as BCs at the HSI. The geometries of the RP-SiC and the axially finned HX configurations were included into the computational domain to simulate the flow of air by using CFD. Temperature- and pressure-dependent physical properties of air were taken from the NIST REFPROP database[35] and implemented as described in the Supporting Information. The parameters of the HX configurations are summarized in Table 2 whereas information relative to meshing can be found in the Supporting Information.

Table 2. Parameters of the HX configurations implemented into the simulations of the salt separator. For the fluidized-bed HX, only the outer-wall temperature and the bed-to-wall heat-transfer coefficient were used in the simulations, further information is given for completeness.

| HX type | Parameter | Heat-transfer effectiveness | | |
		92%	95%	96%
fluidized bed	outer-wall temperature [K]	731.13	728.14	727.17
	bed-to-wall heat-transfer coeff. [$W\,m^{-2}\,K^{-1}$]	624.69	997.63	1238.6
	outer diameter [mm]	101	139	231
	particle size [μm]	180	110	69
	particle material	SiC	Al_2O_3	Al_2O_3
axially finned	number of fins	32	40	40
	fin thickness [mm]	0.8	0.8	0.8
	outer diameter [mm]	97	69	72
RP-SiC	outer diameter [mm]	170	150	140

do not provide a uniform axial temperature profile at the HSI. However, the temperature differences visible at the outer separator wall become smaller towards the centerline. From the inlet to the exit of the dip tube ($x = 634$ mm), all centerline temperatures are equal. Below the dip-tube exit, however, in the part of the salt separator where the salts separate, the centerline temperature profiles of the RP-SiC and axially finned tubular HXs are lower compared to the target temperature profile. Consequently, when heating the salt separator with these RP-SiC and axially finned tubular HX configurations, a lower salt-separation effectiveness must be expected.[11]
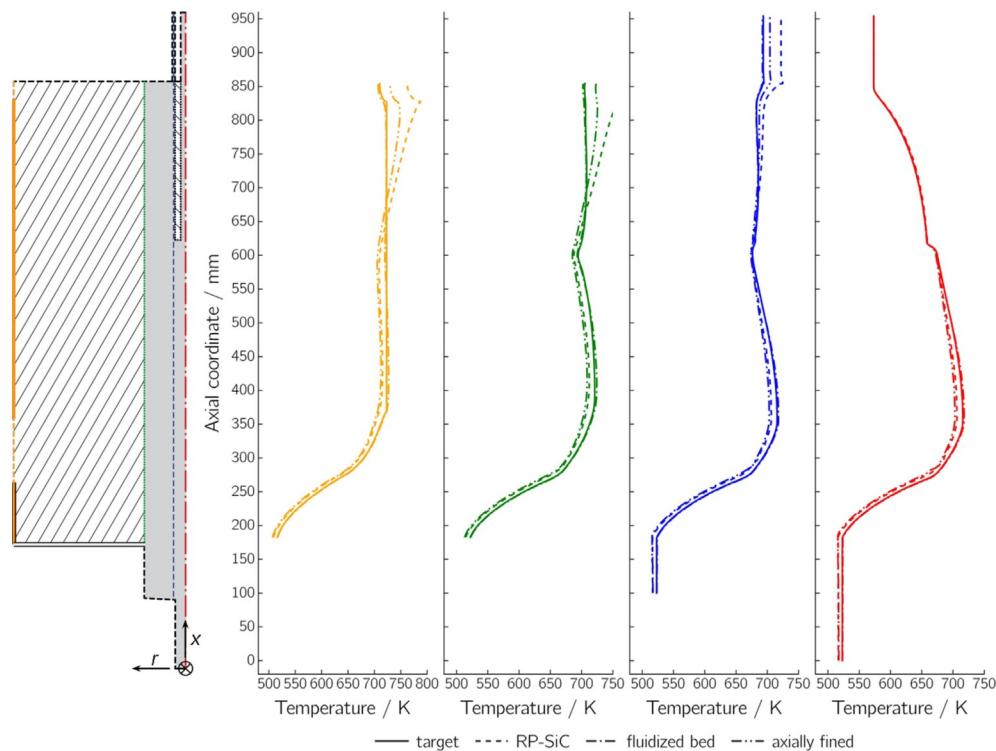
Figure 7. Axial temperature profiles corresponding to the three HX types and the HSI temperature of 723.15 K (the later designated as target temperature profiles). The axial temperature profiles are shown at four radial positions indicated by the colored vertical lines in the sketch of the salt separator (from left to right): outer separator wall ($r=25$ mm), inner separator wall ($r=6$ mm), top outlet of the salt separator ($r=1.71$ mm), and centerline ($r=0$ mm); the colors of the temperature profiles correspond to those of the vertical lines indicating the radial positions in the separator sketch.

Refinement of the axially finned tubular and RP-SiC HX configurations

To increase the centerline temperature profiles corresponding to axially finned tubular and RP-SiC HXs and thus to improve the agreement with the target temperature profile and achieve the desired salt-separation effectiveness, the axially finned tubular and RP-SiC HX configurations have to provide a higher HSI temperature and heat-transfer rate compared to the fluidized-bed HXs. To identify such configurations, the following strategy was applied:

1. Repeated the CFD simulation described earlier for an HSI temperature of 743.15 K, resulting in a heat-transfer rate of 400 W.
2. Carried out preliminary designs of the axially finned tubular and RP-SiC HX for this new set of BCs.
3. Carried out integrated HX/salt separator simulations for these configurations to compute the centerline temperature profiles (discretization of the HX domains used for the simulations in this section are provided in the Supporting Information). The deviation from the target centerline temperature profile was quantified by the maximum centerline temperature deviation,
$\Delta T_{max} = \max(T_{CL,config}) - \max(T_{CL,target})$,
where $T_{CL,config}$ is the centerline temperature profile of the considered HX configuration and $T_{CL,target}$ is the target centerline temperature profile.

4. Computed the refined BCs that would ideally correspond to $\Delta T_{max} = 0$ K by linear interpolation between maximum temperature deviations corresponding to the 723.15 and 743.15 K BCs.

Table 3. BCs for the preliminary design of axially finned tubular and RP-SiC HX configurations and corresponding maximum temperature deviation from the target center temperature profile.

BCs [$T_{HSI}/\dot{Q}_{max}$]	ΔT_{max}	BCs [$T_{HSI}/\dot{Q}_{max}$]	ΔT_{max}
Axially finned tubular HX		*RP-SiC HX*	
723.15 K	−23 K	723.15 K	−13 K
359 W		359 W	
743.15 K	22 K	743.15 K	23 K
400 W		400 W	
Refined BCs			
733.15 K	−5 K	730.15 K	−7 K
380 W		374 W	

Table 4. Design parameters of the refined axially finned tubular and RP-SiC HX configurations corresponding to 95% heat-transfer effectiveness.

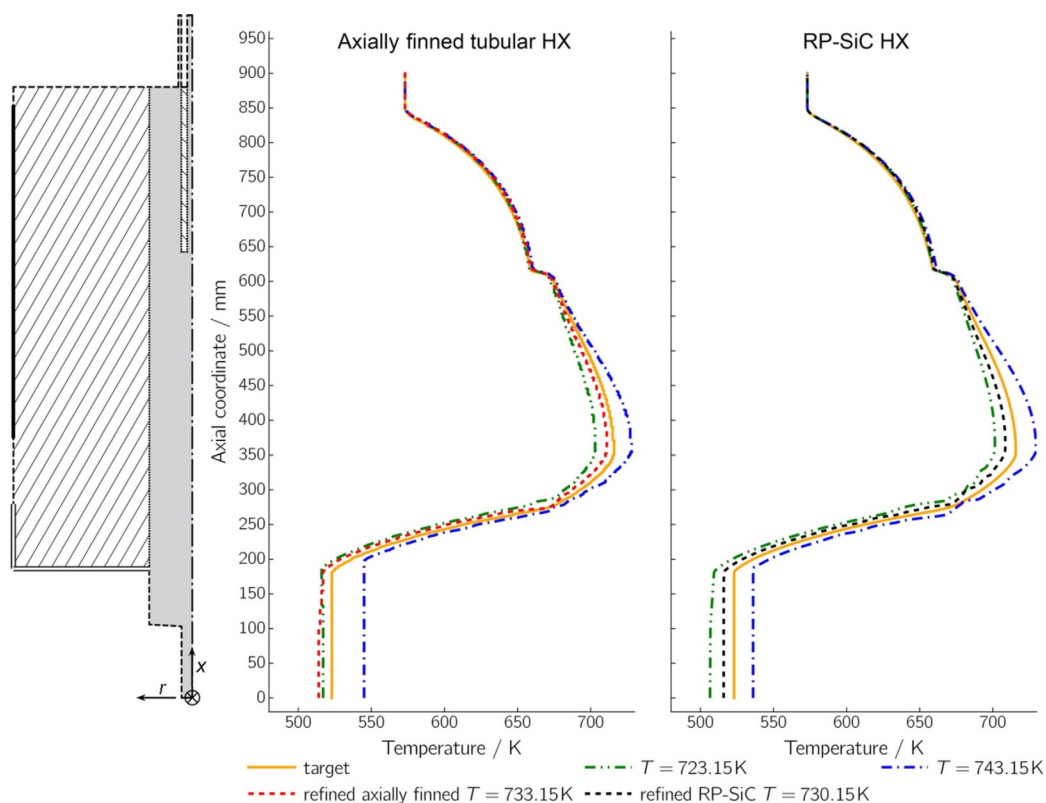| HX type	Design parameter	Value
axially finned	number of fins	40
	fin thickness [mm]	0.8
	outer diameter [mm]	82
RP-SiC	outer diameter [mm]	134

Figure 8. Comparison of the target centerline temperature profile with the profiles corresponding to the 95%-effectiveness configurations of axially finned tubular and RP-SiC HXs designed using HSI temperatures of 723.15 and 743.15 K, and refined HSI temperatures of 733.15 K for the axially finned tubular HX and 730.15 K for the PR-SiC HX.

5. Carried out the preliminary designs of the axially finned tubular and RP-SiC HXs for the refined BCs, computed the corresponding centerline temperature profiles, and calculated the actual maximum temperature deviations for the refined configurations.

The refinement was carried out for the 95%-effectiveness configurations; results are listed in Table 3.

The design parameters for the refined axially finned tubular and the RP-SiC HX configurations are shown in Table 4.

Figure 8 demonstrates that the HX configurations corresponding to the refined BCs lead to improved agreement with the target centerline temperature profile for both axially finned tubular and RP-SiC HXs, respectively. Using another refinement iteration, it should be possible to improve this agreement even further.

Pumping power

Figure 9 compares normalized pumping power versus heat-transfer effectiveness for all HX types considered in this study. For the axially finned tubular and RP-SiC HXs, the configurations corresponding to the refined BCs are shown. As before, for a given HX type and heat-transfer effectiveness, only the configuration with the lowest pumping power is shown. Although for the ranges of parameters investigated

in this study all configurations attain similar maximum effectiveness, the estimated pumping power of the fluidized-bed
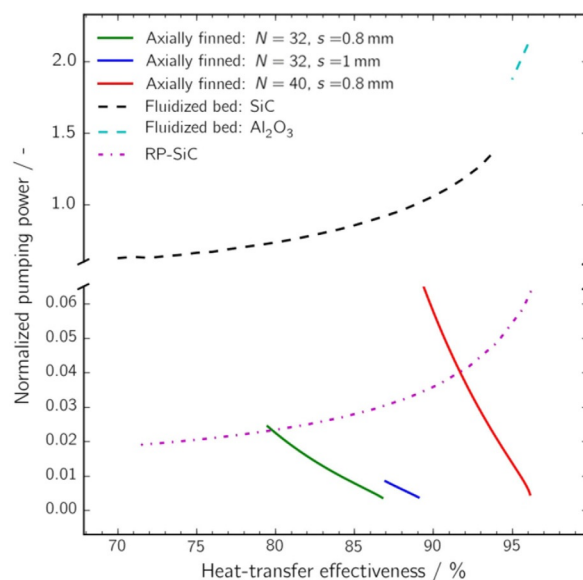

Figure 9. Comparison of the normalized pumping power as a function of heat-transfer effectiveness for the fluidized-bed, RP-SiC, and axially finned tubular HXs. For RP-SiC and axially finned tubular HXs, the configurations corresponding to the refined BCs are shown. For each HX, the configurations with the lowest normalized pumping power are shown. Symbols denoting the individual HX configurations are omitted for improved readability.

Table 5. Comparison of estimated and simulated pumping powers for 95 % heat-transfer effectiveness.

HX	Pumping power [W]	
	preliminary design	simulation
RP-SiC	1.38	1.21
axially finned tubular	0.35	0.15

configurations is roughly two orders of magnitude higher than those of the axially finned tubular and RP-SiC HX configurations.

For the refined RP-SiC and axially finned configurations with 95 % effectiveness, the pumping power was additionally calculated from the simulations according to Equation (2) (this was not possible for the fluidized-bed configurations as the air flow was not computed for this configuration). In Table 5, these values are compared to the pumping power estimated as part of the preliminary design of those HX configurations.

For the RP-SiC HX, the pumping powers estimated for the preliminary design and calculated from the simulation agree well. For the axially finned tubular HX, the pumping power obtained from the simulation is more than two times lower compared to the value estimated for the preliminary design. This discrepancy could be caused by approximating the axially finned tube with a hydraulic diameter to calculate the pressure drop. It means that the pumping power consumed by the axially finned tubular HX is in reality lower than the values shown in Figure 9. The results imply that from the standpoint of the energy input required to pump the air, the axially finned tubular HX is the preferred type of HX, followed closely by the RP-SiC HX, but clearly preferred over the fluidized-bed HX.

Conclusions and Outlook

We investigated the suitability of fluidized-bed, reticulated-porous-SiC (RP-SiC), and axially finned tubular heat exchangers (HXs) to transfer solar energy to a dip-tube salt separator of the hydrothermal gasification (HTG) process using air as heat-transfer fluid (HTF). We showed that the targeted centerline temperature profile for effective salt separation can be reached with an axially uniform temperature profile at the heater/separator interface (HSI) and identified suitable fluidized-bed HX configurations that provide this temperature profile and the corresponding heat-transfer rate at the HSI. Preliminary configurations of the axially finned tubular and RP-SiC HXs were identified using the same HSI temperature profile and heat-transfer rate although these HX types in reality provide a non-uniform temperature profile at the HSI. Computational fluid dynamics (CFD) simulations of selected HX/salt-separator configurations showed that the so-designed axially finned tubular and RP-SiC HXs provide a lower centerline temperature profile than targeted. However, with subsequent refinement of the HX configurations, the agreement with the targeted centerline tempera-

ture profile was improved. It can thus be concluded that it is possible to use all of the considered HX types to heat the salt separator in a way that effects salt separation. Using simple engineering calculations to identify preliminary HX configurations and subsequent refining these configurations using CFD simulations is much less computationally expensive compared to computing the heat transfer inside the salt separator using CFD for several HX configurations and subsequently identify those that provide the targeted centerline temperature profile. We found that the axially finned tubular and RP-SiC HXs require similar power for pumping the HTF whereas the required pumping power for the fluidized bed HX is about two orders of magnitude higher.

The conclusions of this work were obtained using water as feedstock rather than real biomass. It is plausible to expect that the temperature profile in the salt separator will be different when feeding wet biomass. However, for the comparison of different HXs, the error incurred by approximating biomass with pure water is expected to be similar for all considered HXs and thus unlikely to significantly influence the findings of this work.

For the axially finned tubular HX, the discrepancy between the pumping power estimated as part of the preliminary design and that calculated from the simulation should be investigated further. Furthermore, the HX/salt separator should be included in a process study to identify the HX configuration that results in the most economic layout for a solar-heated HTG process. Further work should be carried out to identify conditions leading to the effective separation of type-2 salts to be able to process feedstock such as algae[36] or manure.[37] Modelling work of the salt separator should be advanced to include the separation of type-1 and type-2 salts as well as the effects of fouling of the salt separator due to depositing type-2 salt particles. Development of a physical property model for aqueous, salt-containing biomass slurries would also be helpful for further modelling and other work related to HTG.

List of Symbols

A [m^2]	Surface/Area
χ [−]	Heat-transfer effectiveness
c_p [J kg^{-1} K^{-1}]	Specific heat capacity
d [m]	Diameter
Δp [Pa]	Pressure drop
ΔT [K]	Temperature difference
ε [−]	Void fraction
$\in$ [−]	Hemispherical total emissivity
η_o [−]	Fin efficiency
g [m s^{-2}]	Gravity
h [W m^{-2} K^{-1}]	Heat-transfer coefficient
H [m]	Fin height
k [W m^{-1} K^{-1}]	Thermal conductivity
L [m]	Height
$\dot{m}$ [kg s^{-1}]	Mass flow
$\underline{n}$ [−]	Normal vector
N [−]	Number of fins

p [Pa]	Pressure
P [W]	Pumping power
Π [–]	Normalized pumping power
q [W m^{-2}]	Heat flux
$\dot{Q}$ [W]	Heat-transfer rate
r [m]	Radius
ρ [kg m^{-3}]	Density
s [m]	Fin thickness
S [m^2]	Surface
σ [m^2 kg s^{-2} K^{-1}]	Boltzmann constant
T [K]	Temperature
U [m s^{-1}]	Velocity
$\underline{U}$ [m s^{-1}]	Velocity vector
$\dot{V}$ [m^3 s^{-1}]	Volumetric flow rate
x [m]	Axial position

List of Subscripts

CL	Centerline
config	Configuration
g	Gas
HSI	Heater/separator interface
ht	Heat transfer
i	In/Inner
∞	bulk
max	Maximum
mf	Minimum fluidization
o	Out/Outer
OW	Outer wall
p	Particle
s	Solid
sp	Set point
w	Wall

Conflict of interest

The authors declare no conflict of interest.

[1] a) A. A. Peterson, F. Vogel, R. P. Lachance, M. Fröling, M. J. Antal, J. W. Tester, *Energy Environ. Sci.* **2008**, *1*, 32–65; b) P. Basu, *Biomass Gasification and Pyrolysis*, Elsevier, Amsterdam, **2010**; c) G. W. Huber, S. Iborra, A. Corma, *Chem. Rev.* **2006**, *106*, 4044–4098.

[2] a) R. E. H. Sims, W. Mabee, J. N. Saddler, M. Taylor, *Bioresour. Technol.* **2010**, *101*, 1570–1580; b) S. Srinivasan, *Renewable Energy* **2009**, *34*, 950–954; c) F. Vogel in *Handbook of Green Chemistry, Vol. 2* (Eds.: P. Anastas, R. H. Crabtree), Wiley-VCH, Weinheim, **2009**, pp. 281–324.

[3] A. G. Haiduc, M. Brandenberger, S. Suquet, F. Vogel, R. Bernier-Latmani, C. Ludwig, *J. Appl. Phycol.* **2009**, *21*, 529–541.

[4] a) S. Heyne, M. Seemann, T. J. Schildhauer in *Synthetic Natural Gas from Coal and Dry Biomass, and Power-to-Gas Applications, 1st ed.* (Eds.: T. J. Schildhauer, S. M. A. Biollaz), Wiley, Hoboken, **2016**, pp. 5–40; b) S. K. Sansaniwal, K. Pal, M. A. Rosen, S. K. Tyagi, *Renewable Sustainable Energy Rev.* **2017**, *72*, 363–384.

[5] F. Vogel, in *Synthetic Natural Gas from Coal, Dry Biomass, and Power-to-Gas Applications, 1st ed.* (Eds.: T. J. Schildhauer, S. M. A. Biollaz), Wiley, Hoboken, **2016**, pp. 249–278.

[6] G. Schuster, G. Löffler, K. Weigl, H. Hofbauer, *Bioresour. Technol.* **2001**, *77*, 71–79.

[7] F. Vogel, M. H. Waldner, A. A. Rouff, S. Rabe, *Green Chem.* **2007**, *9*, 616–619.

[8] "Biomass Ash Characteristics and Behaviour in Combustion Systems":S. van Loo, J. Koppejan in *The Handbook of Biomass Combustion and Co-Firing* (Eds.:S. van Loo, J. Koppejan), Earthscan, London, **2012**, pp. 249–288 .

[9] M. Hodes, P. A. Marrone, G. T. Hong, K. A. Smith, J. W. Tester, *J. Supercrit. Fluids* **2004**, *29*, 265–288.

[10] A. Mian, A. A. Ensinas, G. Ambrosetti, F. Marechal, *Chem. Eng. Trans.* **2013**, *35*, 1009–1014.

[11] M. Schubert, J. W. Regler, F. Vogel, *J. Supercrit. Fluids* **2010**, *52*, 99–112.

[12] M. Schubert, J. W. Regler, F. Vogel, *J. Supercrit. Fluids* **2010**, *52*, 113–124.

[13] a) A. A. Peterson, P. Vontobel, F. Vogel, J. W. Tester, *J. Supercrit. Fluids* **2008**, *43*, 490–499; b) A. A. Peterson, P. Vontobel, F. Vogel, J. W. Tester, *J. Supercrit. Fluids* **2009**, *49*, 71–78.

[14] S. M. Heilmann, L. R. Jader, M. J. Sadowsky, F. J. Schendel, M. G. von Keitz, K. J. Valentas, *Biomass Bioenergy* **2011**, *35*, 2526–2533.

[15] A. G. Chakinala, W. P. M. van Swaaij, S. R. A. Kersten, D. de Vlieger, K. Seshan, D. W. F. W. Brilman, *Ind. Eng. Chem. Res.* **2013**, *52*, 5302–5312.

[16] a) M. Schubert, J. Aubert, J. B. Müller, F. Vogel, *J. Supercrit. Fluids* **2012**, *61*, 44–54; b) J. Reimer, F. Vogel, *RSC Adv.* **2013**, *3*, 24503–24508.

[17] G. T. Hong, W. R. Killilea, T. B. Thomason, (Modar Inc.), US 4822497, **1989**.

[18] Ansys Inc., *Ansys CFX 14.5.7*, **2012**, www.ansys.com.

[19] E. Macas, Personal communication, 28 August 2013.

[20] M. Schubert, Personal communication, 12 June 2017.

[21] E. De Boni, Personal communication, 30 June 2015.

[22] D. Kunii, O. Levenspiel, *Fluidization Engineering, 2nd ed.*, Butterworth-Heinemann, Boston, **1991**.

[23] G. Zanganeh, A. Pedretti, S. Zavattoni, M. Barbato, A. Steinfeld, *Sol. Energy* **2012**, *86*, 3084–3098.

[24] F. P. Incropera, D. P. DeWitt, T. L. Bergman, A. S. Lavine, *Fundamentals of Heat and Mass Transfer, 6th ed.*, Wiley, Hoboken, **2007**.

[25] *Handbook of Fluidization and Fluid-Particle Systems* (Ed.: W. C. Yang), Marcel Dekker, New York, **2003**.

[26] H. Martin, *Chem. Eng. Process.* **1984**, *18*, 199–223.

[27] a) G. Flamant, D. Gauthier, H. Benoit, J.-L. Sans, R. Garcia, B. Boissière, R. Ansart, M. Hemati, *Chem. Eng. Sci.* **2013**, *102*, 567–576; b) P. Auerkari, *Mechanical and Physical Properties of Engineering Alumina Ceramics*, VVT Technical Research Centre of Finnland, **1996**, www.vtt.fi/inf/pdf/tiedotteet/1996/T1792.pdf.

[28] "Longitudinal Fin Double-Pipe Exchangers":A. D. Kraus, A. Aziz, J. Welty in *Extended Surface Heat Transfer*, Wiley, Hoboken, **2001**.

[29] TPS Technitube Röhrenwerke GmbH, *Product Catalog*, **2014**, http://www.tps-technitube.com/downloads/inosindt/inosindt_pdf_extended_surface_tubes_3.pdf.

[30] a) I. Ghosh, *J. Heat Transfer* **2009**, *131*, 101004; b) D. A. Nield, A. Bejan, *Forced Convection, 4th ed.*, Springer, New York, **2013**.

[31] a) I. Hischier, P. Poživil, A. Steinfeld, *J. Sol. Energy Eng.* **2012**, *134*, 011004; b) R. G. Munro, *J. Phys. Chem. Ref. Data* **1997**, *26*, 1195–1203; c) P. Pozivil, S. Ackermann, A. Steinfeld, *J. Sol. Energy Eng.* **2015**, *137*, 064504.

[32] V. Calmidi, R. Mahajan, *J. Heat Transfer* **2000**, *122*, 557–565.

[33] Numerical Modelling GmbH, *NM-SESES Multiphysics FEM solver*, **2017**, www.nmtec.ch.

[34] J. L. Lage in *Transport Phenomena in Porous Media* (Eds.: D. B. Incham, I. Pop), Pergamon, Oxford, **1998**, pp. 1–30.

[35] E. W. Lemmon, M. L. Huber, M. O. McLinden, *NIST Standard Reference Database 23: Reference Fluid Thermodynamic and Transport Properties-REFPROP, Version 9.1*, National Institute of Standards and Technology, Standard Reference Data Program, Gaithersburg, **2013**, https://www.nist.gov/refprop.

[36] J. A. Onwudili, A. R. Lea-Langton, A. B. Ross, P. T. Williams, *Bioresour. Technol.* **2013**, *127*, 72–80.

[37] M. H. Waldner, PhD thesis, ETH Zurich, **2007**.